MDPI

Article

Complex Bioactive Chitosan–Bioglass Coatings on a New Advanced TiTaZrAg Medium–High-Entropy Alloy

Andrei Bogdan Stoian [1], Radu Nartita [1], Georgeta Totea [2], Daniela Ionita [1,*] and Cristian Burnei [3]

1 Department of General Chemistry, Faculty of Chemical Engineering and Biotechnologies, University Politehnica of Bucharest, 313 Splaiul Independentei, 060042 Bucharest, Romania; andreibstoian@yahoo.com (A.B.S.); nartita.radu@gmail.com (R.N.)
2 Buftea Obstetrics and Gynecology Hospital, M. Burghele Hospital, Studiolului 5, 070000 Buftea, Romania; georgeta.totea@gmail.com
3 Clinical Department of Orthopedics and Traumatology II, Clinical Emergency Hospital, Calea Floreasca 8, 014461 Bucharest, Romania; cristian.burnei@umfcd.ro
* Correspondence: daniela.ionita@upb.ro

Abstract: High-entropy alloys (HEAs), also known as multicomponent or multi-principal element alloys (MPEAs), differ from traditional alloys, which are usually based only on one principal element, in that they are usually fabricated from five or more elements in large percentages related to each other, in the range of 5%–35%. Despite the usually outstanding characteristics of HEAs, based on a properly selected design, many such alloys are coated with advanced composites after their elaboration to further improve their qualities. In this study, 73Ti-20Zr-5Ta-2Ag samples were covered with chitosan and a mixture of chitosan, bioglass, and ZnO particles to improve the materials' antibacterial properties. A variety of methods, including scanning electron microscopy, atomic force microscopy, and mechanical and electrochemical determinations, has permitted a quantified comparison between the coated and uncoated surfaces of this medium–high-entropy alloy. The materials' properties were enhanced by the complex coating, giving the alloys not only high antibacterial activity, but also good corrosion protection.

Keywords: bioactive; antibacterial; chitosan; high-entropy alloy; titanium alloy

1. Introduction

The introduction of multi-principal metal alloys (MPEAs) [1] as new materials with high performance properties has been an answer to the needs involved in the development of new technologies. Initially, such alloys were divided based on their entropy values into high-entropy alloys (HEA) and medium-entropy alloys (MEAs) [2,3]. The research design concept of such materials permits the development of alloys with proposed desired characteristics that promote safety and sustainability in a large variety of scientific fields, despite the fact that they were initiated for use in extreme conditions. This possibility has presented an opportunity for new HEAs and MEAs to be used not only in technological fields that use extreme environmental conditions, but also in biomedical sciences in which specific properties related to biocompatibility are needed [4].

Compared to traditional metallic biomaterials already in use, such as TiAlV, TiAlNb, and TiAlFe, HEA and MEA materials based on Ti [5–8] have high strength, superior corrosion resistance, and a Young's modulus close to that of the human bone, thus avoiding stress shielding. Various new alloys have been fabricated and their potential application in bioapplications investigated in the last five years [9–11], and, more recently, they have been included in the term "bioHEA" [12].

Ti, Ta, Zr, and Ag are known for their biocompatibility and antibacterial properties [13] in various systems, and in multielement alloys such as 73Ti-20Zr-5Ta-2Ag, a synergic process is expected to take place, thus increasing antibacterial activity.

Configurational entropy values have been used to classify materials as high-entropy (>1.5 R), medium-entropy (1–1.5 R), and low-entropy (<1 R) [14]. The classification of high entropy as >1.5 R matches the internal energy per mole of a monoatomic ideal gas, which is equal to 1.5 RT. According to this classification, the 73Ti-20Zr-5Ta-2Ag alloy used in this study, which has a calculated entropy of 1.26 R, can be classified as a medium–high-entropy alloy.

Despite the fact that bioHEAs were elaborated with a design that offers better performances, surface modifications have been applied to further improve their response at the bio-interface. There have been numerous paths to implement surface modifications of metallic implant materials based on titanium, but two stand out as the most frequently used: electrochemical anodization, which led to the formation of different porous structures such as nanotubes that improve electrochemical stability, cell response, and antibacterial effects [15–17]; and coatings based on different organic (various polymers) and inorganic materials (hidroxyapatite, bioglass).

Composite organic–inorganic materials have attracted interest in the orthopedic field, because they combine the mechanical properties of the organic component with the bioactivity of inorganic components. Moreover, the coating process can be achieved at room temperature, and additional active components, such as antibiotics, proteins, and enzymes, can be included in the polymeric matrix during the coating process [18,19].

Chitosan, as a biodegradable polymer, is inherently biocompatible and functional. In a composite material, it can contribute to defined interactions and tailored properties, such as the balance between hydrophilic/hydrophobic characteristics and antibacterial effects [20]. Chitosan is a natural cationic polysaccharide polymer derived from chitin that has been widely used as the organic component of organic–inorganic composite coatings. It has numerous useful properties that allow it to be used in different biomedical applications, such as its antibacterial properties and cytocompatibility with varying types of cells [21].

Bioactive glass was discovered by Hench and coworkers in the late 1960s. It was dubbed 45S5 or "Bioglass" [22]. Bioactive glasses are a class of material that can form chemical bonds with surrounding tissues through the formation of hidroxyapatite layers that make the glass essential for biomedical applications [23].

Zinc is necessary for bone growth in the human body and is the most bountiful minor element present in human bone [24,25]. Adding ZnO to the bioactive glass matrix can produce higher chemical stability, stimulate cell proliferation and differentiation, and facilitate the development of durable bonding with the bone [26].

Numerous methods have proven successful to be used for the deposition of bioactive surface coatings. Ceramic coatings on implant materials can be deposited by techniques such as chemical vapor deposition (CVD) [27], physical vapor deposition (PVD) [28], or plasma electrolytic oxidation (PEO) [29], which can be used to control the properties of the obtained coating to a certain degree. These techniques usually employ high temperatures that make the deposition of organic components such as polymers, antibiotics, or proteins hard to achieve. Chitosan can be successfully deposited using plasma treatments of the substrate, which still raises challenges [30]. It can also be used in electrochemical deposition, which in turn can be used for the fabrication of chitosan–ceramic composite coating [31].

To tackle the limitations associated with high processing temperatures of the plasma-based coating systems, and to minimize the risk of ionic species interfering with the coating during the electrochemical processes, this study uses the doctor blade method for the coating process. This method is a fast, simple, scalable way to create uniform thin films, with little solution wastage during deposition.

The present work aimed to prepare composite coatings based on chitosan, bioglass, and ZnO on a bioHEA substrate, as in a previous work focused on the composite's design and characterization [32]. Further, we complete this characterization by investigating electrochemical stability and highlighting different mechanisms that control the different properties of this composite, such as adherence and antibacterial action. Such data could

provide important knowledge for the future design of other biopolymer–bioglass composite coatings on high-entropy alloys that meet specific bioapplication needs.

2. Materials and Methods

Samples of 73Ti-20Zr-5Ta-2Ag alloy [33] (20 mm-diameter disks) were polished with SiC paper with increasing grits from P800 to P4000 (Buehler, Lake Bluff, IL, USA) and cleaned successively with acetone, ethanol, and distilled water for 10 min each in an ultrasonic bath, then etched by immersion in an acid mixture of $3HNO_3$:$1HF$:$2H_2O$ (*v*/*v*/*v*) for 10 s.

Half a gram of chitosan (190–310 kDa, 78%–85% deacetylation, Sigma-Aldrich, Saint Louis, MO, USA) was dissolved in 1% acetic acid aqueous solution and stirred for 6 h. An amount of 2.5 mg bioglass (BG-BG-45S5, 0.2–250 μm) and 2.5 mg ZnO (<50 nm) were added to 10 mL of the previously prepared chitosan solution. The mixture was magnetically stirred for 1 h, then ultrasonicated for 1 h.

Three types of samples were produced for this work: etched 73Ti-20Zr-5Ta-2Ag alloy (P1), etched 73Ti-20Zr-5Ta-2Ag alloy covered with chitosan solution (P2), and etched 73Ti-20Zr-5Ta-2Ag alloy covered with the chitosan + BG + ZnO mixture (P3).

For the fabrication of sample types P2 and P3, the doctor blade method was employed. Briefly, the alloy disk edges were masked with Teflon tape, the solutions were placed on the metallic surface of the alloy, and a blade was used to remove the excess solution. The samples were left to dry in atmosphere, and the tape was subsequently removed.

The morphology of the samples was analyzed by scanning electron microscopy (SEM) using a Hitachi SU 8230 (HITACHI High-Technologies Corporation, Tokyo, Japan) with an accelerating voltage of 10 kV, a chamber pressure of approx. 8×10^{-4} Pa, and a working distance of approx. 9 mm. The microscope was equipped with an energy-dispersive X-ray (EDS) analyzer (Oxford Instruments, Abingdon, UK).

The force–distance (F-Z) curves and average roughness values were evaluated using an A.P.E. Research A100-SGS atomic force microscope (AFM, A.P.E. Research, Trieste, Italy) from 5 measurements for each sample.

The adhesion of the films to the substrate was determined by pull-off tests using an PosiTest AT-M adhesion tester (DeFelsko, Ogdensburg, NY, USA). The samples were fixed on 10 mm-diameter aluminum dollies with double-adhesive tape. The presented data represent the necessary force to detach the films from the alloy substrates.

Electrochemical determinations were performed with a PGSTAT100N potentiostat (Metrohm Autolab, Barendrecht, The Netherlands) in 0.9% NaCl with three-electrode cells that consisted of samples used as working electrodes, Ag/AgCl as a reference, and a Pt sheet as a counter electrode. Electrochemical impedance spectroscopy (EIS) was performed at opened-circuit potential (OCP) in the range of 10^4–10^{-1} Hz at 10 mV amplitude and corrosion monitoring (Tafel plots) at ±200 mV vs. OCP.

The samples were mounted in a cell that left an area of 1 cm^2 of the working electrode uncovered. They were left in the electrolyte for 15 min, until a state of equilibrium was reached. An aqueous solution of 0.9% NaCl was used, since it is related to body fluid. An amount of 0.9% NaCl contains approximately the same concentration of Cl^- ions, which are the most likely species to cause metal corrosion. Furthermore, 0.9% NaCl has the same surface tension as living tissue [34].

The antibacterial effect was tested against two common pathogens involved in implant-related infections: Escherichia coli (Gram-negative rod) and Staphylococcus aureus (Gram-positive coccus). We used two standardized strains, *E. coli* ATCC 25922 (American Type Culture Collection) and *S. aureus* ATCC 25923, obtained after 24 h incubation on Columbia Agar + 5% sheep blood at 37 °C. The microbial suspensions were adjusted to 0.5 McFarland units. The tested materials were placed in sterile polypropylene tubes after being subjected to 10 min UV treatment, then covered with 10 mL bacterial suspension. Positive and negative controls were prepared in PPE tubes, one containing a bacterial suspension and the other sterile saline. All tubes were incubated at 37 °C for 24–72 h, and periodically,

the absorbance was read at 600 nm against a negative control using a UVISON 1700 spectrophotometer (UVISON Technologies Limited, Sevenoaks, Kent, UK). The growth inhibition index was computed using the formula [35]:

$$I\% = \frac{(C_n - C_0) - (T_n - T_0)}{(C_n - C_0)} \cdot 100 \tag{1}$$

where *I* is the growth inhibition index, *C* is the optical density (OD_{600}) of the positive control read before incubation and after *n* hours ($n = 24, 36, 48, 60,$ and 72 h), and *T* is the OD_{600} of inoculum in contact with the samples before and after incubation at selected time intervals. All readings were performed in triplicate.

3. Results and Discussion

3.1. Surface Morphology

The surface of sample P1 (Figure 1a) showed that the etched 73Ti-20Zr-5Ta-2Ag alloy was covered with oxides produced during the etching process. The grooves and ridges are representative of an oxidized TiZr alloy [36]. Small pores with diameters around 400–500 nm were observed sporadically on the surface of the sample. The oxide structures formed on the surface are most likely the result of the mechanisms involved in the formation of self-organized nanostructures on valve metals in electrolytes containing fluoride ions, which include competitive processes between oxide formation and fluorine complexes dissolution [37]. Clusters of silver particles were visible on the surface of the sample as lighter-colored formations. Sample P2 (Figure 1b) had a surface uniformly covered with the chitosan solution. No oxide formations were found to protrude from the film. The different colored stripes represent different film thicknesses resulting from the blading process. Sample P3 (Figure 1c) had a surface uniformly covered with ceramic particles embedded in the polymeric matrix. The smaller particles (200–300 nm) show that the ZnO particles had a tendency to agglomerate during the deposition or drying process [38]. The larger particles (500–2500 nm) are the components of bioglass. The bioglass particles deposited on the surface were smaller than those used in the suspension, hinting that the larger particles were subjected to faster sedimentation in the suspension before deposition [39].

Energy-dispersive X-ray spectroscopy (EDS) was used to determine the composition of the surfaces of the samples. In Figure 2, the elemental maps of the analyzed samples are presented. Sample P1 (Figure 2a) had a surface uniformly covered with Ti and Zr oxides. Clusters of Ag were identified on the surface, probably as a result of the alloy's heterogeneity. On sample P2 (Figure 2b), the thickness of the chitosan film prevents the direct visualization of the substrate; however, the Ti and Zr oxides are present beneath. The results obtained for sample P3 (Figure 2c) showed the oxidized substrate covered with the chitosan film in which ceramic particles were embedded. The particles had a uniform dispersion on the surface. Components of bioglass were identified on the surface, the largest particles being formed of SiO_2, and smaller particles of uniformly dispersed CaO and P_2O_5. EDS analysis confirmed the ZnO particles' tendency to agglomerate.
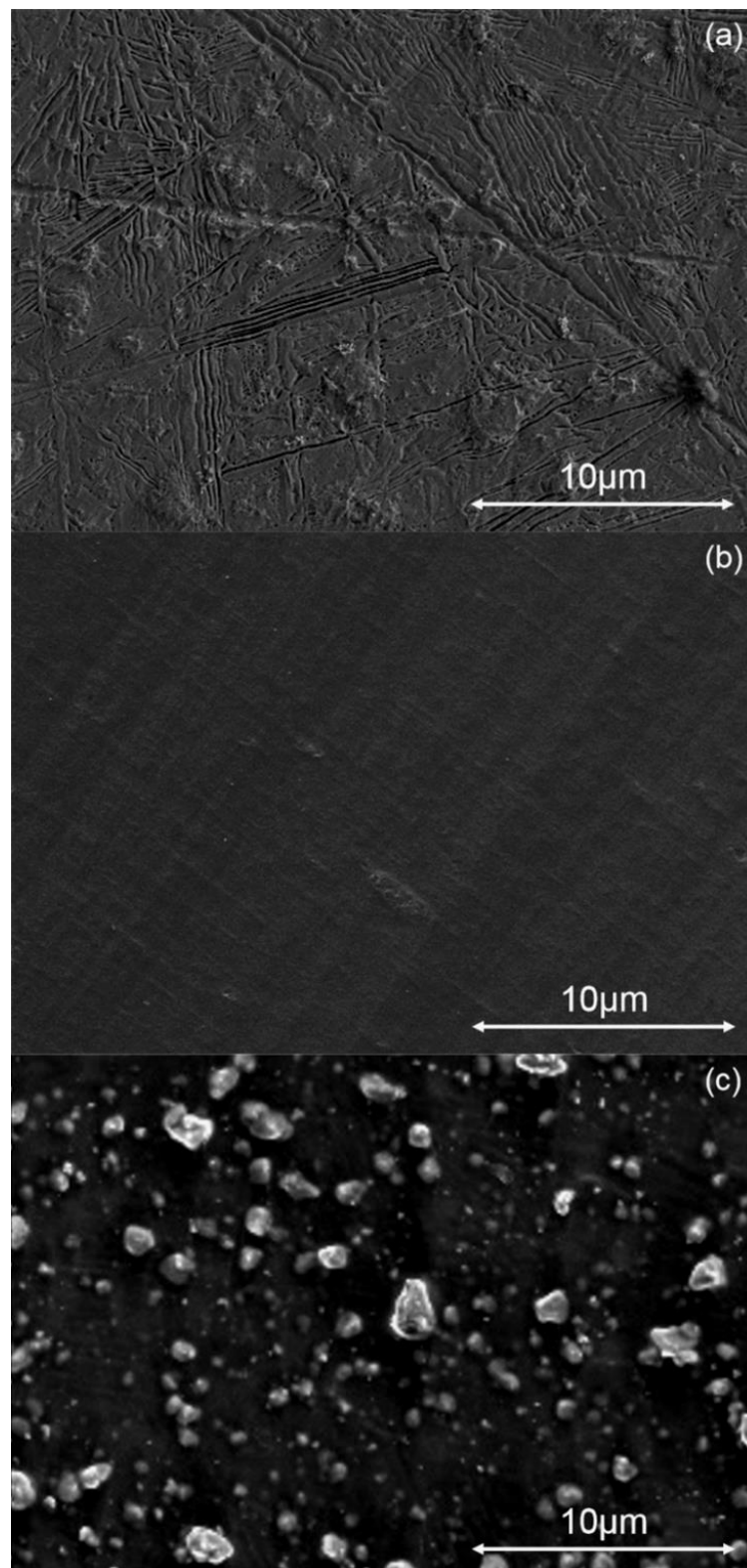
Figure 1. SEM micrographs for (**a**) P1; (**b**) P2; (**c**) P3.
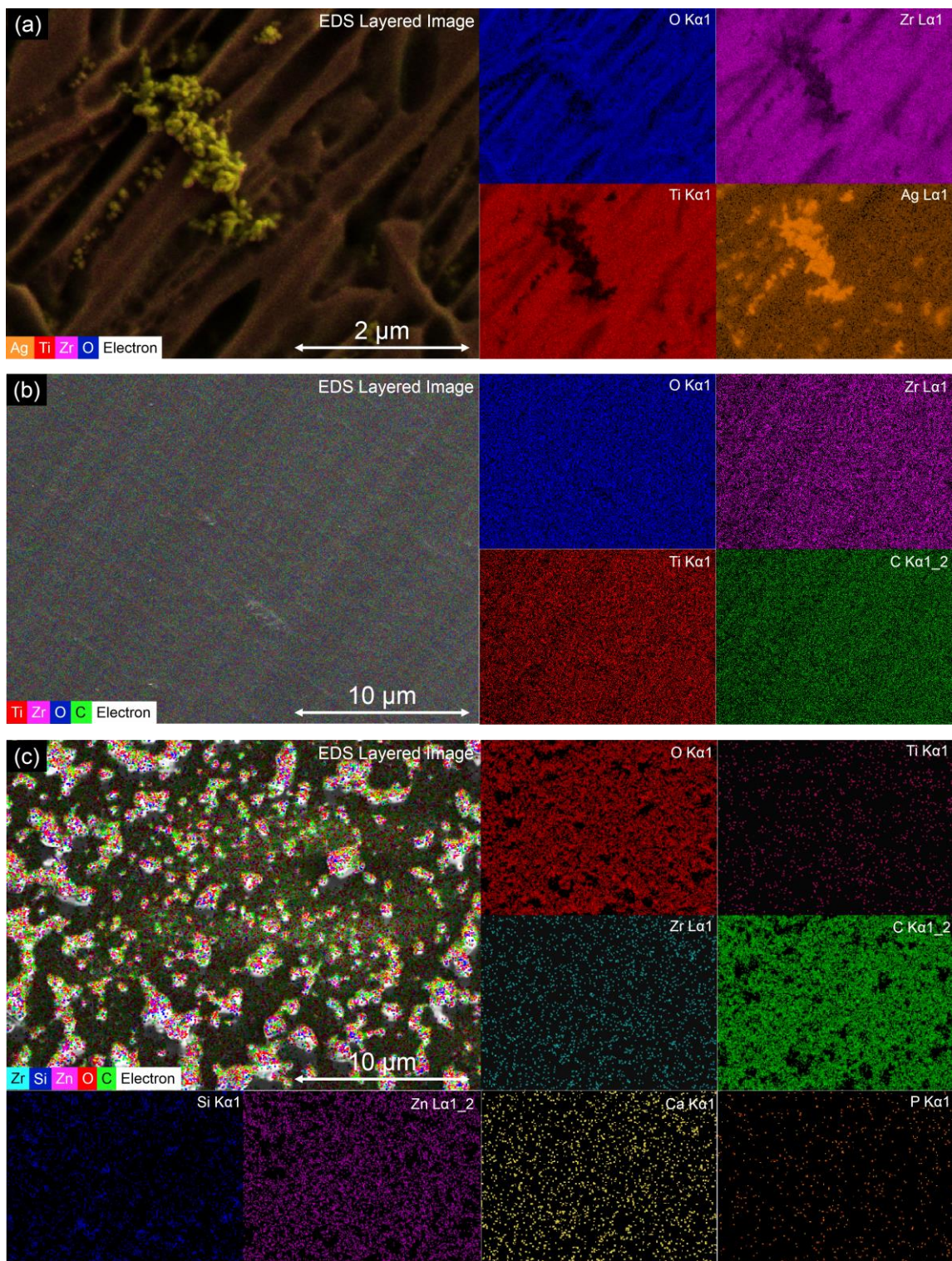
Figure 2. EDS mapping for (**a**) P1; (**b**) P2; (**c**) P3.

The normalized median values of AFM tip-sample adhesion forces were calculated from the tip deflection and are shown as F-Z diagrams in Figure 3. Sample P1 had the highest adhesion force of 24 ± 3 nm and a short activity range, which can be attributed to the relatively smooth and tough oxide surface. Sample P2 had the lowest adhesion force of 6 ± 2 nm, but it had the longest range of activity, probably given by the semi-elastic properties of the chitosan film deposited on the surface. Sample P3 gave mixed results

depending on the material that the AFM tip touched during the experiments, with a median value of 16 ± 4 nm being between the values of samples P1 and P2.
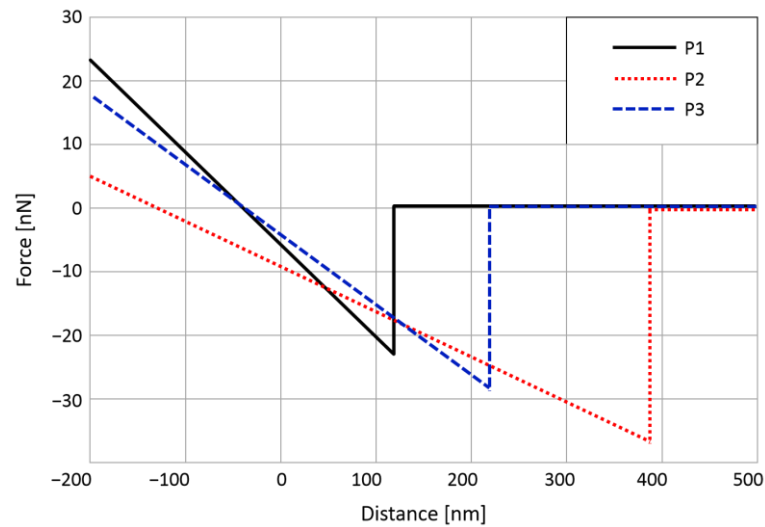

Figure 3. F-Z curves of normalized median values of AFM tip-sample adhesion forces.

The roughness values (Figure 4) were in accordance with the SEM topography images. The roughness decreased from 0.9 to 0.6 µm when the alloy was covered with the chitosan film and increased to 1.4 µm when the mixture containing chitosan, bioglass, and ZnO was added to the surface. Combined with the results obtained from the F-Z curves, this means that the bioglass and ZnO particles were not completely covered by the polymeric matrix, but just partly embedded. This effect can be attributed to a shrinking of the film during the drying process.
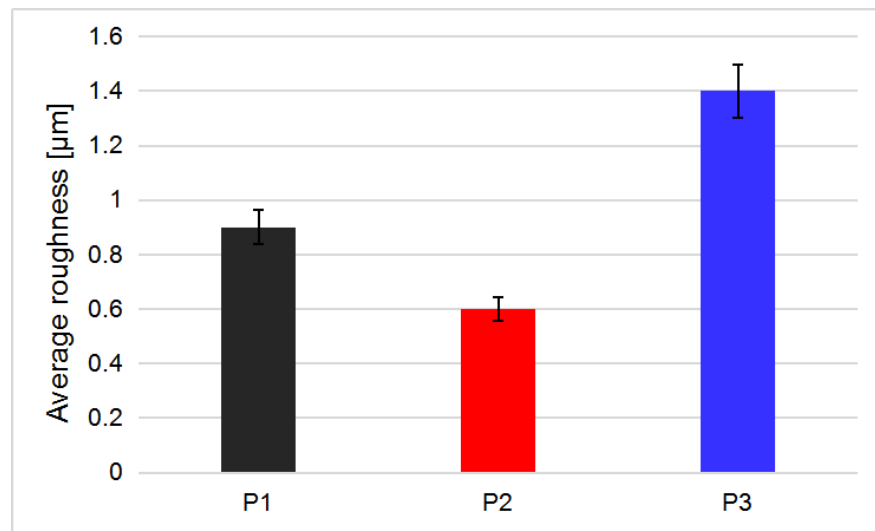

Figure 4. Average roughness values of the analyzed samples.

The adhesion forces of the films on the analyzed samples (Figure 5) show that the chitosan film (P2) did not adhere well to the TiZrTaAg substrate. For sample P1, the data represent the detachment of the outer oxide layer from the substrate. The addition of BG and ZnO to the chitosan solution (P3) led to an increase in the adhesion force of the composite film on the substrate. The addition of BG and ZnO enhanced the mechanical properties of the film, possibly by mechanically reinforcing the polymeric coating with metal oxide particles, or by the formation of chemical bonds [40] between the chitosan

and metallic oxide particles due to nanoparticle–matrix interface interactions and the high volume-to-mass ratios of these particles.
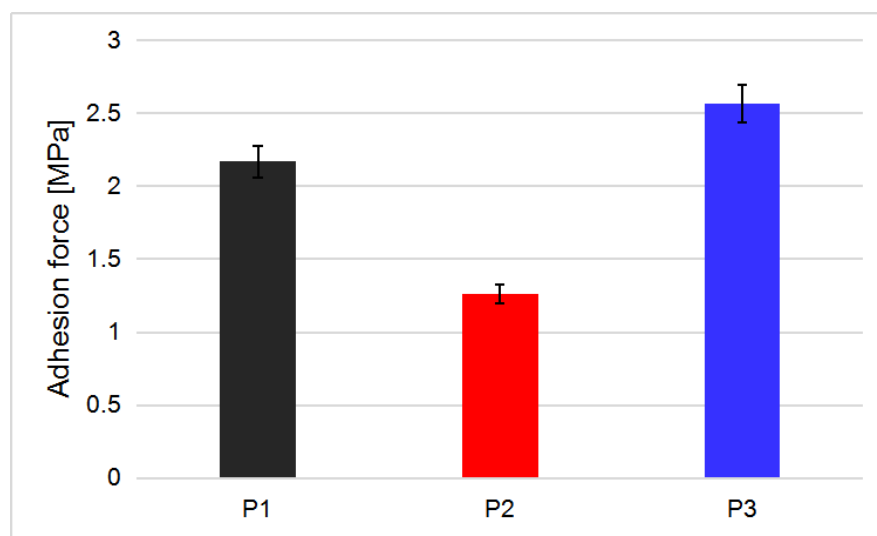

Figure 5. Adhesion forces of the films on the substrate.

3.2. Electrochemical Characterization

EIS data are shown as Nyquist and Bode plots along with the equivalent circuits used to fit the data in Figure 6, and the parameters of the equivalent circuit elements are shown in Table 1. The samples have different behaviors when exposed to a corrosive medium depending on the surface coating. For sample P1, the (Rx-Ox) couple might be associated with a resistive and pseudo-capacitive process at the interface between the electrolyte and the oxide layer. The Qh element was added to represent the heterogeneous characteristics of the oxide layer. For sample P2, a Warburg impedance element was needed to fit the data, hinting that a diffusion-controlled charge transfer takes place at the coating–substrate interface [41]. The behavior of the oxide film described by the parallel elements (Rx-Qx) attributed to the oxide film in sample P1 is masked in sample P2 by the addition of chitosan, which completely covers the oxide structures and fills the pores, thus becoming (Rf-Qf-Wf). Sample P3 shows the most complex behavior, given by the multitude of elements present on the surface. In the Bode Phase plot, the two humps represent the differentiation of the phases present in the coating. Thus, a more complicated circuit was needed to fit the data. The (Rf-Cf-Wf) couple represents the entirety of the coating, containing chitosan, bioglass, and ZnO particles through which the charge transfer takes place at the interface between the electrolyte, and the coating and the (Rx-Qx) couple represents the oxide film on the substrate.

Potentiodynamic polarization tests were used to evaluate the corrosion behavior of the samples in 0.9% NaCl. The data are presented as Tafel plots (Figure 7), and the corrosion parameters are presented in Table 2. A small decrease in the corrosion current and the corrosion rate was observed when comparing samples P1 and P2. This can be attributed to the filling of the imperfections present in the oxide layer with the chitosan film. Sample P3 showed the greatest corrosion resistance and the lowest corrosion current, hinting that the bioglass and ZnO nanoparticles dispersed in the polymeric matrix have a major role in corrosion protection [42].
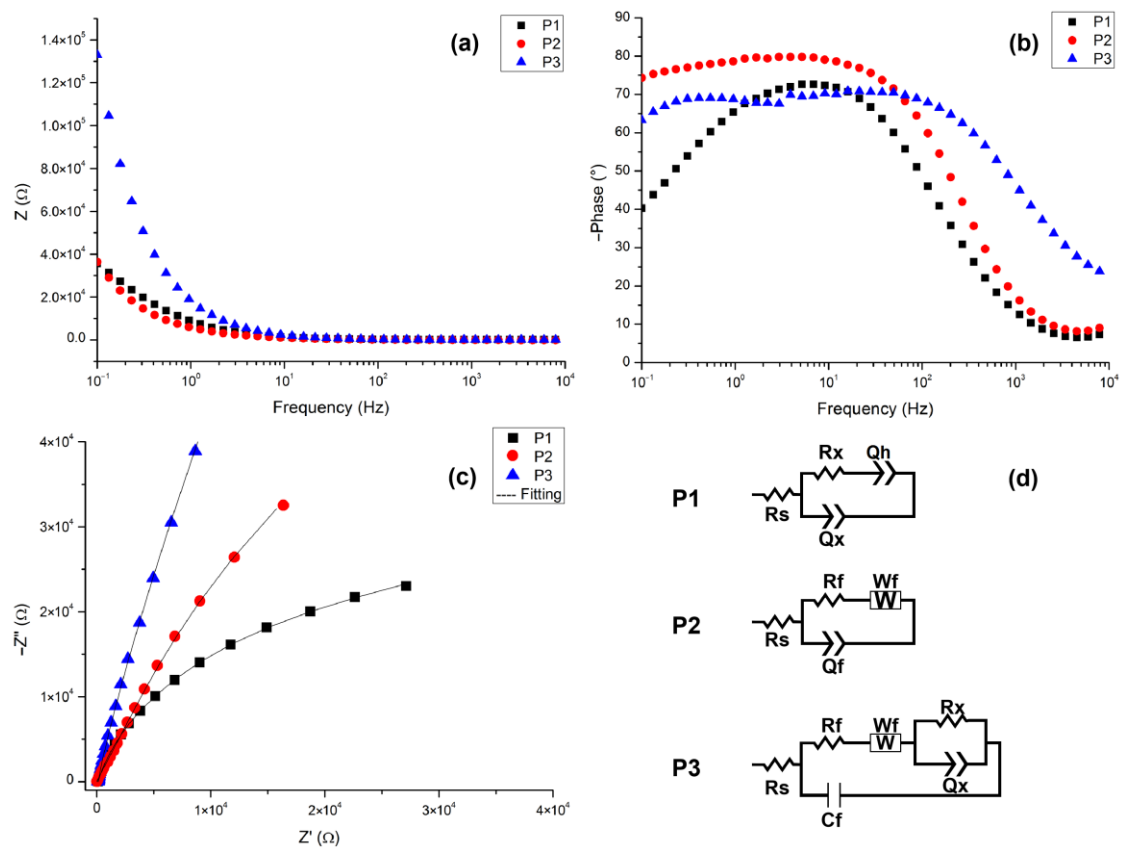
Figure 6. Bode Modulus (**a**), Bode Phase (**b**), Nyquist plots (**c**), and equivalent circuits used to fit the EIS data (**d**) for the analyzed samples.
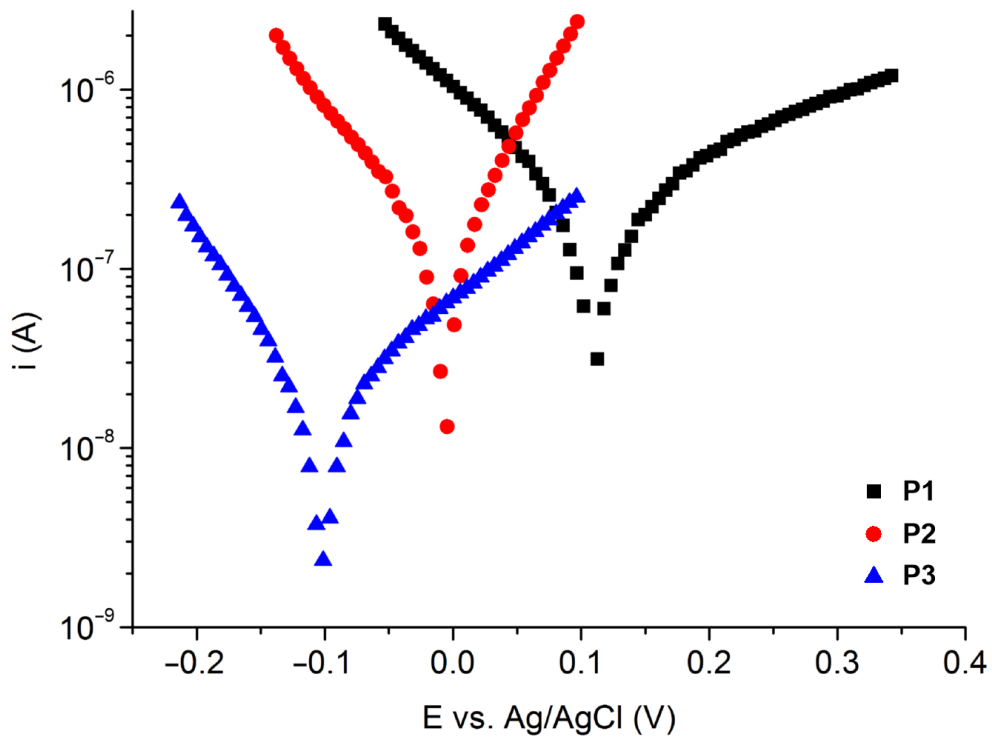

Figure 7. Tafel plots of the analyzed samples.

Table 1. Parameters of equivalent circuit elements.

Element	P1	P2	P3
Rs (Ω cm^2)	109	110	84
Rx $\times$ 10^6 (Ω cm^2)	1.08	-	13.1
Qx (μF/cm$^2 \cdot$s^{n-1})	21.5	-	18.5
n_{Qx}	0.84	-	0.88
Qh (μF/cm$^2 \cdot$s^{n-1})	76.1	-	-
n_{Qh}	0.64	-	-
Rf $\times$ 10^6 (Ω cm^2)	-	2.3	1.4
Qf (μF/cm$^2 \cdot$s^{n-1})	-	9.26	-
n_{Qf}	-	0.918	-
Cf (μF/cm^2)	-	-	31.7
Wf (Ω cm^2)	-	2.2	43.8
χ^2	0.018289	0.031125	0.0090866

Table 2. Corrosion parameters calculated from the Tafel plots.

Element	P1	P2	P3
Ecorr (V)	0.107	−0.0056	−0.108
Icorr $\times$ 10^{-9} (A)	355.74	132.8	34.24
Vcorr $\times$ 10^{-3} (mm/year)	9.76	3.64	0.64
Polarization resistance $\times$ 10^6 (Ω)	1.56	1.65	14.34
βa (V/dec)	0.160	0.260	0.405
βc (V/dec)	0.134	0.142	0.128

3.3. Antibacterial Activity

As shown in Figure 8a,b, the first reading of OD$_{600}$ was made after 24 h, followed by subsequent readings at the specified time intervals. It was observed that the OD$_{600}$ starts to decrease continuously for all samples in the interval of 24–48 h, and then it begins to slowly rise again for the next 24 h. The most effective antibacterial activity for all materials was observed after 48 h of incubation. As the OD$_{600}$ is lower, the bacterial growth is also low. The slow rise in OD$_{600}$ after 60 and 72 h means that the materials' antibacterial activity starts to decrease as time passes, the maximum activity being at 48 h. The ZnO and bioglass particles present in the coating of sample P3 successfully inhibited bacterial growth by 83% in the case of *S. aureus* and 75% in case of *E. coli* at 48 h. All the materials had antibacterial activity (Figure 8c), but the highest was presented by sample P3.

The slightly better results obtained for *S. aureus* vs. *E. coli* can be attributed to differences in the membranes of the two organisms. The Gram-positive bacteria have a multilayered outer peptidoglycan membrane, whereas the Gram-negative bacteria have two outer-layer membranes with a layer of peptidoglycan. Furthermore, the ZnO particles have abrasive textures that can destroy the bacterial membrane [43].
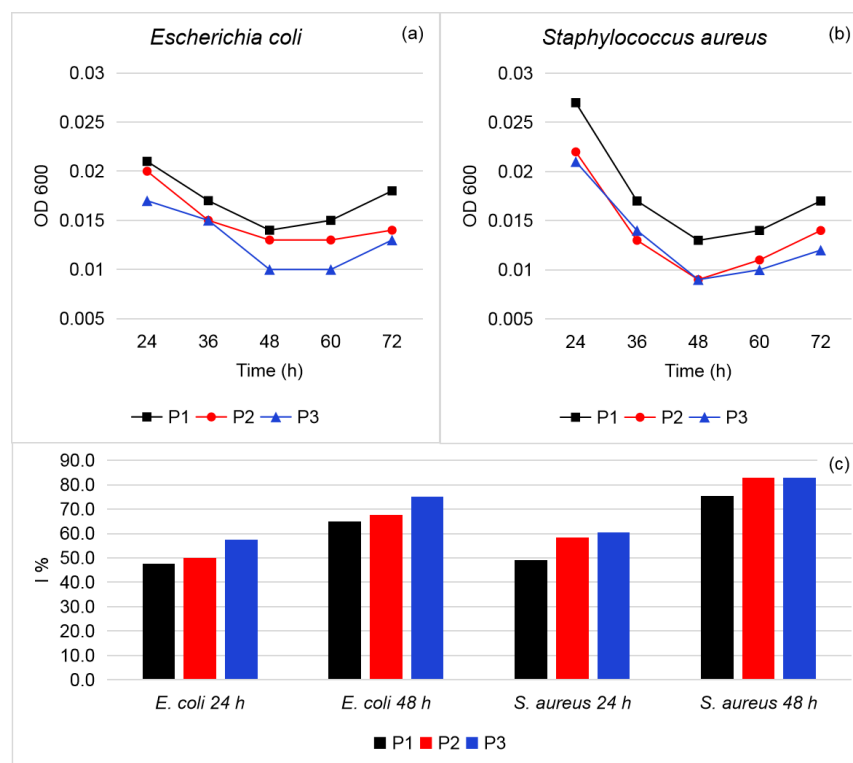
Figure 8. Antibacterial activity against (**a**) *E. coli* and (**b**) *S. aureus*; (**c**) bacterial growth inhibition index for the analyzed samples.

4. Conclusions

Etched 73Ti-20Zr-5Ta-2Ag alloy samples were coated by the doctor blade method with chitosan and with a mixture composed of chitosan, bioglass, and ZnO particles. SEM and EDS analysis revealed that the coated samples had good homogeneity. The AFM readings revealed that the chitosan coating had the largest force range and the lowest roughness, and that the bioglass and ZnO nanoparticles were partially embedded in the polymeric matrix, giving the samples a large roughness value. The addition of bioglass and ZnO particles to chitosan enhanced the mechanical properties of the coating by physicochemical interactions and increased the adhesion force of the film by 100%. Electrochemical testing revealed that the addition of bioglass and ZnO particles to chitosan has a beneficial effect for corrosion protection, and that a charge transfer takes place at the interface between the coating and the substrate. The corrosion resistance was improved by an order of magnitude when the chitosan + BG + ZnO film was coated on the 73Ti-20Zr-5Ta-2Ag alloy. The antibacterial effect was good for all samples, with the best result being given by the combination of chitosan with bioglass and ZnO particles. The antibacterial effect was 10% higher against *S. aureus* than *E. coli.*

Further studies will be performed on 73Ti-20Zr-5Ta-2Ag in order to test other coatings for potential uses in other fields.

Author Contributions: Conceptualization, D.I.; methodology, D.I. and C.B.; software, R.N.; validation, D.I. and C.B.; formal analysis, R.N., A.B.S. and G.T.; investigation, D.I.; resources, D.I.; data curation, D.I. and C.B.; writing—original draft preparation, A.B.S. and G.T.; writing—review and editing, R.N.; visualization, D.I.; supervision, D.I.; project administration, D.I.; funding acquisition, D.I. All authors have read and agreed to the published version of the manuscript.

Institutional Review Board Statement: Not applicable.

Informed Consent Statement: Not applicable.

Data Availability Statement: Not applicable.

Conflicts of Interest: The authors declare no conflict of interest.

References

1. Yeh, J.W.; Chen, S.K.; Lin, S.J.; Gan, J.Y.; Chin, T.S.; Shun, T.T.; Tsau, C.H.; Chang, S.Y. Nanostructured high-entropy alloys with multiple principal elements: Novel alloy design concepts and outcomes. *Adv. Eng. Mater.* **2004**, *6*, 299–303. [CrossRef]
2. Nartita, R.; Ionita, D.; Demetrescu, I.; Enachescu, M. A fresh perspective on medium entropy alloys applications as coatings or coating substrate. *Annal. Acad. Rom. Sci. Ser. Phys. Chem.* **2022**, *7*, 34–46. [CrossRef]
3. Son, S.; Lee, D.; Kwon, H.; Moon, J.; Park, K.B.; Kim, A.; Choi, J.; Jeong, J.; Cho, S.; Kim, H.S. Microstructure and mechanical properties of equiatomic Ti-containing medium-entropy alloys. *J. Alloys Compd.* **2023**, *935*, 168089. [CrossRef]
4. de Oliveira, T.G.; Fagundes, D.V.; Capellato, P.; Sachs, D.; da Silva, A.A.A.P. A Review of Biomaterials Based on High-Entropy Alloys. *Metals* **2022**, *12*, 1940. [CrossRef]
5. Vyavahare, S.; Mahesh, V.; Mahesh, V.; Harursampath, D. Additively manufactured meta-biomaterials: A state-of-the-art review. *Compos. Struct.* **2023**, *305*, 116491. [CrossRef]
6. Wong, K.K.; Hsu, H.C.; Wu, S.C.; Ho, W.F. Structure and properties of Ti-rich Ti–Zr–Nb–Mo medium-entropy alloys. *J. Alloys Compd.* **2021**, *868*, 159137. [CrossRef]
7. Nguyen, V.T.; Qian, M.; Shi, Z.; Song, T.; Huang, L.; Zou, J. A novel quaternary equiatomic Ti-Zr-Nb-Ta medium entropy alloy (MEA). *Intermetallics* **2018**, *101*, 39–43. [CrossRef]
8. Raducanu, D.; Vasilescu, E.; Cojocaru, V.D.; Cinca, I.; Drob, P.; Vasilescu, C.; Drob, S.I. Mechanical and corrosion resistance of a new nanostructured Ti–Zr–Ta–Nb alloy. *J. Mech. Behav. Biomed. Mater.* **2011**, *4*, 1421–1430. [CrossRef]
9. Geanta, V.; Voiculescu, I.; Istrate, B.; Vrânceanu, D.; Ciocoiu, R.; Cotruț, C. The influence of chromium content on the structural and mechanical properties of AlCrxFeCoNi high entropy alloys. *Int. J. Eng. Res. Afr.* **2018**, *37*, 23–28. [CrossRef]
10. Motallebzadeh, A.; Peighambardoust, N.S.; Sheikh, S.; Murakami, H.; Guo, S.; Canadinc, D. Microstructural, mechanical and electrochemical characterization of TiZrTaHfNb and Ti1.5ZrTa0.5Hf0.5Nb0.5 refractory high-entropy alloys for biomedical applications. *Intermetallics* **2019**, *113*, 106572. [CrossRef]
11. Yuan, Y.; Wu, Y.; Yang, Z.; Liang, X.; Lei, Z.; Huang, H.; Wang, H.; Liu, X.; An, K.; Wu, W.; et al. Formation, structure and properties of biocompatible TiZrHfNbTa high-entropy alloys. *Mater. Res. Lett.* **2019**, *7*, 225–231. [CrossRef]
12. Hori, T.; Nagase, T.; Todai, M.; Matsugaki, A.; Nakano, T. Development of non-equiatomic TiNbTaZrMo high-entropy alloys for metallic biomaterials. *Scr. Mater.* **2019**, *172*, 83–87. [CrossRef]
13. Lemire, J.; Harrison, J.; Turner, R. Antimicrobial activity of metals: Mechanisms, molecular targets and applications. *Nat. Rev. Microbiol.* **2013**, *11*, 371–384. [CrossRef] [PubMed]
14. Murty, B.S.; Yeh, J.-W.; Ranganathan, S. *High Entropy Alloys*; Elsevier Science & Tech. Butterworth-Heinemann Ltd.: Oxford, UK, 2014.
15. Portan, D.; Ionita, D.; Demetrescu, I. Monitoring TiO$_2$ nanotubes elaboration condition, a way for obtaining various characteristics of nanostructures. *Key Eng. Mater.* **2009**, *415*, 9–12. [CrossRef]
16. Grigorescu, S.; Pruna, V.; Titorencu, I.; Jinga, V.V.; Mazare, A.; Schmuki, P.; Demetrescu, I. The Two Step Nanotube Formation on TiZr as Scaffolds for Cell growth. *Bioelectrochemistry* **2014**, *98*, 39–45. [CrossRef] [PubMed]
17. Berger, J.E.; Jorge, A.M., Jr.; Asato, G.H.; Roche, V. Formation of self-ordered oxide nanotubes layer on the equiatomic TiNbZrHfTa high entropy alloy and bioactivation procedure. *J. Alloys Compd.* **2021**, *865*, 158837. [CrossRef]
18. de Jonge, L.T.; Leeuwenburgh, S.C.; Wolke, J.G.; Jansen, J.A. Organic–inorganic surface modifications for titanium implant surfaces. *Pharm. Res.* **2008**, *25*, 2357–2369. [CrossRef]
19. Simchi, A.; Tamjid, E.; Pishbin, F.; Boccaccini, A. Recent progress in inorganic and composite coatings with bactericidal capability for orthopaedic applications. *Nanomed. Nanotechnol. Biol. Med.* **2011**, *7*, 22–39. [CrossRef]
20. Duan, Q.; Chen, Y.; Yu, L.; Xie, F. Chitosan–Gelatin Films: Plasticizers/Nanofillers Affect Chain Interactions and Material Properties in Different Ways. *Polymers* **2022**, *14*, 3797. [CrossRef]
21. Rabea, E.I.; Badawy, M.E.-T.; Stevens, C.V.; Smagghe, G.; Steurbaut, W. Chitosan as antimicrobial agent: Applications and mode of action. *Biomacromolecules* **2003**, *4*, 1457–1465. [CrossRef]
22. Hench, L.L.; Splinter, R.J.; Allen, W.; Greenlee, T. Bonding mechanisms at the interface of ceramic prosthetic materials. *J. Biomed. Mater. Res.* **1971**, *5*, 117–141. [CrossRef]
23. Maximov, M.; Maximov, O.-C.; Craciun, L.; Ficai, D.; Ficai, A.; Andronescu, E. Bioactive Glass—An Extensive Study of the Preparation and Coating Methods. *Coatings* **2021**, *11*, 1386. [CrossRef]
24. Ishikawa, K.; Miyamoto, Y.; Yuasa, T.; Ito, A.; Nagayama, M.; Suzuki, K. Fabrication of Zn containing apatite cement and its initial evaluation using human osteoblastic cells. *Biomaterials* **2002**, *23*, 423–428. [CrossRef] [PubMed]
25. Li, X.; Wang, X.; He, D.; Shi, J. Synthesis and characterization of mesoporous CaO–MO–SiO$_2$–P$_2$O$_5$ (M = Mg, Zn, Cu) bioactive glasses/composites. *J. Mater. Chem.* **2008**, *18*, 4103–4109. [CrossRef]
26. Hoppe, A.; Mouriño, V.; Boccaccini, A.R. Therapeutic inorganic ions in bioactive glasses to enhance bone formation and beyond. *Biomater. Sci.* **2013**, *1*, 254–256. [CrossRef] [PubMed]

27. Faÿ, S.; Kroll, U.; Bucher, C.; Vallat-Sauvain, E.; Shah, A. Low pressure chemical vapour deposition of ZnO layers for thin-film solar cells: Temperature-induced morphological changes. *Sol. Energy Mater. Sol.* **2005**, *86*, 385–397. [CrossRef]
28. Salehi, S.; Kharaziha, M.; Salehi, M. Multifunctional plasma-sprayed nanocomposite coating based on FA-ZnO-GO with improved bioactivity and wear behaviour. *Surf. Coat. Technol.* **2020**, *404*, 126472. [CrossRef]
29. Schwartz, A.; Kossenko, A.; Zinigrad, M.; Gofer, Y.; Borodianskiy, K.; Sobolev, A. Hydroxyapatite Coating on Ti-6Al-7Nb Alloy by Plasma Electrolytic Oxidation in Salt-Based Electrolyte. *Materials* **2022**, *15*, 7374. [CrossRef]
30. Vesel, A. Deposition of Chitosan on Plasma-Treated Polymers—A Review. *Polymers* **2023**, *15*, 1109. [CrossRef]
31. Jugowiec, D.; Łukaszczyk, A.; Cieniek, L.; Kot, M.; Reczyńska, K.; Cholewa-Kowalska, K.; Pamuła, E.; Moskalewicz, T. Electrophoretic deposition and characterization of composite chitosan-based coatings incorporating bioglass and sol-gel glass particles on the Ti-13Nb-13Zr alloy. *Surf. Coat. Technol.* **2017**, *319*, 33–46. [CrossRef]
32. Prodana, M.; Ionita, D.; Stoian, A.B.; Demetrescu, I.; Mihai, G.V.; Enachescu, M. The design and characterization of new chitosan, bioglass and ZnO-based coatings on Ti-Zr-Ta-Ag. *Coatings* **2023**, *13*, 493. [CrossRef]
33. Vasilescu, E.V.; Calderon, M.J.M.; Vasilescu, C.; Drob, S.I.; Stanciu, D.E.; Ivanescu, S.; Ionita, M.D.; Prodana, M. Ti-Zr-Ta-Ag Bio-alloy for Orthopedic Implants OSIM. Bucuresti. Patent 132031, 30 April 2019.
34. Implants for Surgery (ISO 16429:2004). Available online: https://www.iso.org/obp/ui/#iso:std:iso:16429:ed-1:v1:en (accessed on 1 May 2023).
35. Jaiswal, S.; Duffy, B.; Jaiswal, A.; Stobie, N.; McHale, P. Enhancement of the antibacterial properties of silver nanoparticles using β-cyclodextrin as a capping agent. *Int. J. Antimicrob. Agents* **2010**, *36*, 280–283. [CrossRef] [PubMed]
36. Wang, W.; Cui, W.; Xiao, Z.; Qin, G. The improved corrosion and wear properties of Ti-Zr based alloys with oxide coating in simulated seawater environment. *Surf. Coat. Technol.* **2022**, *439*, 128415. [CrossRef]
37. Anand, A.; Varghese, S.; Kurian, T. Preparation of ultra-fine dispersions of zinc oxide by simple ball-milling: Optimization of process parameters. *Powder Technol.* **2015**, *271*, 187–192. [CrossRef]
38. Li, C.; Ni, Y.; Gong, J.; Song, Y.; Gong, T.; Zhu, X. A review: Research progress on the formation mechanism of porous anodic oxides. *Nanoscale Adv.* **2021**, *4*, 322–333. [CrossRef]
39. Sergi, R.; Bellucci, D.; Cannillo, V. A Comprehensive Review of Bioactive Glass Coatings: State of the Art, Challenges and Future Perspectives. *Coatings* **2020**, *10*, 757. [CrossRef]
40. Li, Y.; Zhou, Y.; Wang, Z.; Cai, R.; Yue, T.; Cui, L. Preparation and Characterization of Chitosan-Nano-ZnO Composite Films for Preservation of Cherry Tomatoes. *Foods* **2021**, *10*, 3135. [CrossRef]
41. Vasconcelos, C.D.; Rocha, A.; Pereira, M.; Fonseca, J. Electrolyte diffusion in a chitosan membrane. *Polym. Int.* **2001**, *50*, 309–312. [CrossRef]
42. John, S.; Joseph, A.; Jose, A.; Narayana, B. Enhancement of corrosion protection of mild steel by chitosan/ZnO nanoparticle composite membranes. *Prog. Org. Coat.* **2015**, *84*, 28–34. [CrossRef]
43. Yusof, N.A.A.; Zain, N.M.; Pauzi, N. Synthesis of ZnO nanoparticles with chitosan as stabilizing agent and their antibacterial properties against Gram-positive and Gram-negative bacteria. *Int. J. Biol. Macromol.* **2019**, *124*, 1132–1136. [CrossRef]